Solidification Map of a Nickel-Base Alloy

J.J. BLECHER, T.A. PALMER, and T. DEBROY

The solidification behavior of the advanced nickel-base alloys, such as Inconel® Alloy 690, is important for understanding their microstructure, properties, and eventual service behavior in nuclear power plant components. Here, an experimental and theoretical program of research is undertaken with the aim of developing a quantitative understanding of the solidification behavior under a wide range of temperature gradients and solidification growth rates. The temperature gradient and solidification rates vary spatially by several orders of magnitude during keyhole mode laser welding. Therefore, the solidification structure is experimentally characterized from microscopic examinations of the resulting fusion zones and correlated with fundamental solidification parameters to provide a widely applicable solidification map that can be employed for a broad range of solidification processes. The cell and secondary dendrite arm spacings are quantitatively correlated with cooling rates. An Alloy 690 solidification map, which illustrates the effect of temperature gradient and solidification rate on the morphology and scale of the solidification structures, is also presented.

I. INTRODUCTION

HIGH performance nickel-base alloys are widely used in industry[1–5] because of their superior structural stability, desirable mechanical properties, and high resistance to stress corrosion cracking. For example, Inconel® Alloy 690, a high chromium content nickel-base alloy, is widely used in installation and repair of the steam generator tubing and pressurized water reactor components.[6] Fabrication and maintenance of these alloy parts require an understanding of their solidification behavior because of its significant impact on the mechanical properties. Unlike well established alloy systems, such as stainless steels,[7] a quantitative understanding of Alloy 690 solidification behavior is not currently available.

Previous studies on the solidification behavior of Alloy 690 have provided useful knowledge about the morphology of the solidification structure. Cellular and columnar dendritic structures were observed in both arc and laser welded fusion zones.[8–13] Characterization of the solidification structures showed that cell spacings and the secondary dendrite arm spacings varied with heat input per unit length during the fabrication process. The scale of the solidification structures were correlated with heat input because the heat input could be accurately determined. However, it is now well established that the heat input does not uniquely define the solidification structure because the same heat input can result in significantly different thermal conditions depending on the fabrication speed and the power used.[14]

The scale of the cells or dendrites depends primarily on the fundamental solidification parameters, such as the temperature gradient (G) and the solidification growth rate (R). The cooling rate can be directly related to the scale of the solidification structures, regardless of the heat input or other attributes of a fabrication process.[15] A morphological map showing solidification structures as a function of fundamental solidification parameters can provide significant benefits to the construction of new power plants and the refurbishment of existing plants. This enhanced understanding of the solidification mechanisms will lead to improved fabrication and performance of Alloy 690 in high temperature applications.

Realistic calculations of the solidification parameters during welding have been enabled by recent advances in numerical modeling. For example, Zhang et al.[16] utilized a heat transfer and fluid flow model and showed that calculated thermal cycles during cooling after arc spot welding agreed well with the corresponding experimental thermal cycles. Rai et al.[17–19] calculated G, R, GR, and the morphology parameter (G/R) at the trailing edge of the weld pool during laser welding of a wide range of alloys. Anderson et al.[5,20] made use of the columnar to equiaxed transition (CET) model[21–23] in order to study stray grain formation in single crystal alloys. Using coupled models, Tan et al.[24] determined the temperature field during laser spot welding of stainless steel to calculate a number of solidification characteristics, such as grain growth direction, morphology, and cell and secondary dendrite arm spacing. Numerical modeling has been used extensively to calculate solidification parameters[5,16–20,24] and to study the solidification behavior of alloys.

In this study, the solidification behavior of a Ni-Cr-Fe alloy, Alloy 690, is investigated based on experimentally determined solidification structure and theoretically

J.J. BLECHER, Ph.D. Candidate, T. DEBROY, Professor, and T.A. PALMER, Associate Professor, are with the Department of Materials Science and Engineering, The Pennsylvania State University, University Park, PA 16802. Contact e-mail: jjb5120@psu.edu

calculated solidification parameters, such as temperature gradients and the solidification growth rates. During microscopic analysis, the laser welds exhibit a wide range of cellular and columnar dendritic structures across the fusion zone. The local temperature gradients and solidification rates during keyhole mode laser welding are calculated with a well-tested numerical heat transfer and fluid flow model. In addition, the scale of cellular and dendritic structures are then correlated to the cooling rates, allowing relations between cooling rate and cell and secondary dendrite arm spacing to be developed. The critical G/R parameter for the transition from cells to dendrites is then determined and used to calculate the area fractions of columnar dendrites in the transverse cross sections of the experimental fusion zones. A solidification map for Alloy 690 is then constructed to predict the formation of cells and dendrites and the scale of the cells and dendrite arms for given values of G and R.

II. EXPERIMENTS AND MODEL DEVELOPMENT

A. *Experimental Welds*

Autogenous bead-on-plate welds were made on 12.7 mm thick Inconel® Alloy 690 plate with an IPG Photonics® YLR-12000-L ytterbium fiber laser. The 1070 to 1100 nm wavelength laser light was directed to the workpiece through a 200 μm process fiber and focused with a YW50 Precitec® welding head. The optics included 200 mm focus length collimating and focusing lenses. Beam characterization with a PRIMES® Focus Monitor confirmed a 200 mm focus length, a 300 μm beam diameter at focus, and a divergence angle of 150 mrad. The focus plane of the laser beam was positioned at the surface of the workpiece with no offset. Laser power varied between 1.0 and 5.6 kW, and travel speed was held constant at 34 mm s^{-1}. The composition of the Alloy 690 plate is shown in Table I.

Standard metallographic techniques were used to prepare transverse sections of the laser welds. Electrolytic etching in 10 wt pct oxalic acid for several seconds revealed the microstructure of the fusion zone and base metal. A Nikon® Epiphot microscope imaged the microstructures at magnifications between 100 and 1000 times magnification. A Nikon® DS-Fi2 camera and Nikon® NIS Elements software were used to capture micrographs. Series of 10 to 30 images at 100 times magnification were stitched together into larger images using Adobe® Photoshop CS5. Secondary dendrite arm spacing, cell spacing, and morphology area measurements were performed with ImageJ software. The linear intercept method was used to measure the

secondary arm spacings and cell spacings. Four measurements per micrograph at 1000 times magnification were used to determine cell spacings for each location and corresponding cooling rate. If one cell spacing measurement fell outside of the mean plus or minus one standard deviation, it was not included in the reported mean. The reported secondary arm spacings are an average of three or more measurements in one 1000 times magnification micrograph. Each dendrite used in the measurement had a minimum of seven arms.

B. *Mathematical Modeling and Solidification Calculations*

The three-dimensional (3D) finite difference based heat transfer and fluid flow model used in this paper has been documented elsewhere in the literature,[17–19,25–28] so only a brief description of the features will be presented here. Calculation of the keyhole profile is done before the heat transfer and fluid flow calculations and is based on the method proposed by Kaplan,[29] which performs a point by point heat balance at the keyhole wall. The profile and resulting heat flux at the keyhole wall are then incorporated into the heat transfer and fluid flow model as a heat source. The equations for the conservation of mass, momentum, and energy are solved for enthalpy and fluid velocity. The resulting temperature fields are used to determine the solidification parameters. The Alloy 690 material properties used for these calculations are shown in Table II.

The heat transfer and fluid flow model has been extensively evaluated and validated for keyhole mode laser beam welding for a variety of materials, including aluminum, stainless steel, tantalum, titanium, vanadium, and structural steel alloys.[17–19] In addition to accurately predicting the experimental weld pool dimensions for various welding powers, speeds, and laser beam profiles, the solidification parameters G, GR, and G/R were calculated at the weld centerline.[18] The model has also been employed to quantitatively study the solidification of austenitic stainless steels[35] and the effect of cooling rate on the primary solidification phase. The calculated and measured thermal cycles and cooling rates agreed, which allowed for the establishment of relations between cooling rates (1000 to 10,000 K s^{-1}) and spacings of primary and secondary dendrites.

The temperature gradient (G) and solidification growth rate (R) are calculated from the temperature field, which is output by the heat transfer and fluid flow model. These parameters, G and R, have been calculated for every position along the solidification front, which is a 3D surface from which the 2D transverse cross-section is extracted. The combined forms of G and R include the cooling rate (GR) and the solidification morphology parameter (G/R). The cooling rate can be directly

Table I. Composition of Alloy 690 Plate

Composition (Wt Pct)	Ni	Cr	Fe	Mn	Si	C	Cu	S
Alloy 690	59.96	29.62	9.68	0.19	0.08	0.03	<0.01	0.004

Table II. Material Properties of Alloy 690 Used in the Calculations

Material Property	Value	Reference
Absorptivity of liquid	0.313	[30]
Density of liquid at the melting point (kg m^{-3})	7500	[31]
Density of liquid at the boiling point (kg m^{-3})	6100	[31]
Viscosity of liquid (kg m^{-1} s^{-1})	0.0051	[31]
Solidus temperature [K (°C)]	1616 (1343)	[32]
Liquidus temperature [K (°C)]	1650 (1377)	[32]
Enthalpy of solid at solidus (kJ kg^{-1})	879	[33]
Enthalpy of liquid at liquidus (kJ kg^{-1})	1200	[33]
Specific heat of solid (J kg^{-1} K^{-1})	665	[33]
Specific heat of liquid (J kg^{-1} K^{-1})	673	[33]
Thermal conductivity of solid (J m^{-1} s^{-1} K^{-1})	33	[34]
Thermal conductivity of liquid (J m^{-1} s^{-1} K^{-1})	46	[31]
Thermal conductivity of liquid at boiling point (J m^{-1} s^{-1} K^{-1})	47	[31]
Coefficient of thermal expansion (K^{-1})	1.0×10^{-6}	[31]
Temperature coefficient of surface tension (mN m^{-1} K^{-1})	-0.37	[31]

related to the size of the features in the fusion zone. The morphology parameter can be used to describe the shape of the solidification structures, such as (from highest G/R value to lowest) planar, cellular, columnar dendritic, and equiaxed dendritic.

In order to calculate G and R, the direction of heat flow at the liquidus temperature must be determined, which is the gradient of the temperature field

$$\nabla T = \frac{\partial T}{\partial x} i + \frac{\partial T}{\partial y} j + \frac{\partial T}{\partial z} k, \qquad [1]$$

where T is temperature and i, j, and k are unit vectors in the x, y, and z direction, respectively. The heat flow direction at a certain position in space is expected to be normal to the 3D liquidus surface. The temperature gradient, G, is

$$G = \|\nabla T\| = \sqrt{\left(\frac{\partial T}{\partial x}\right)^2 + \left(\frac{\partial T}{\partial y}\right)^2 + \left(\frac{\partial T}{\partial z}\right)^2}, \qquad [2]$$

which is simply the magnitude of the vector. The solidification direction is assumed to be aligned opposite to the heat transfer direction. Therefore,

$$\cos \alpha = \frac{-\frac{\partial T}{\partial x}}{\|\nabla T\|}, \qquad [3]$$

where α is the angle between the welding direction and solidification growth direction. In order for the assumption to be valid, the orientation of the easy growth direction, $\langle 100 \rangle$, of the pre-existing grain must be parallel to the solidification direction. In polycrystalline material with randomly oriented grains, this condition is not usually met, however, with mean grain sizes much smaller than the dimensions of the weld, competitive growth will quickly select the best orientation during solidification. The solidification rate, R, is

$$R = U \cos \alpha, \qquad [4]$$

where U is the welding speed. Figure 1(a) shows the relationship between U, R, and α on the 3D solidification surface and the resulting transverse cross-section of the

weld. The variation of α with depth along the central longitudinal plane for a 2.8 kW weld is shown in Figure 1(b). It should be noted that R is also a function of the angle between the easy growth direction of the grain and the welding direction. However, this angle is typically neglected for the case of polycrystalline materials.

III. RESULTS AND DISCUSSION

A. *Microstructural Characterization*

Bead-on-plate laser welds were made on Alloy 690 plates at a travel speed of 34 mm s^{-1} and powers ranging from 1.0 to 5.6 kW. The combination of laser power and welding speed resulted in the formation of a keyhole in each weld. Calculated temperature and fluid velocity fields are shown in Figure 2 for powers of 1.0, 2.8, and 4.7 kW. The boiling [3085 K (2812 °C)], liquidus [1650 K (1377 °C)], and solidus [1616 K (1343 °C)] temperature contours are plotted. The characteristic high depth to width ratio of keyhole mode laser weld pools is observed as is the Marangoni effect driven fluid flow, which drives molten metal to the edges of the pool. As expected, an increase in the laser power produces a larger pool overall. The width of the two phase mushy region also increases, which suggests different thermal cycles along the solidification front. A comparison of the experimental and calculated weld pool dimensions is shown in Figure 3. Good agreement is observed between both sets of values, except at the 5.6 kW width where material expulsion was observed. At powers exceeding 5.6 kW and up to 10.6 kW, significant liquid metal expulsion occurred, indicating the onset of drilling.

Examination of the fusion zone microstructure revealed two distinct morphologies, cells and columnar dendrites, and a range of scales. Figure 4 shows representative micrographs of cells and columnar dendrites in the transverse fusion zone of the 3.8 kW weld. The micrograph of the cells is taken near the root of the weld, where the scale of the cell spacing is about 3 μm due to the relatively high cooling rates. At this location, cell growth occurs in a variety of directions, and the cells
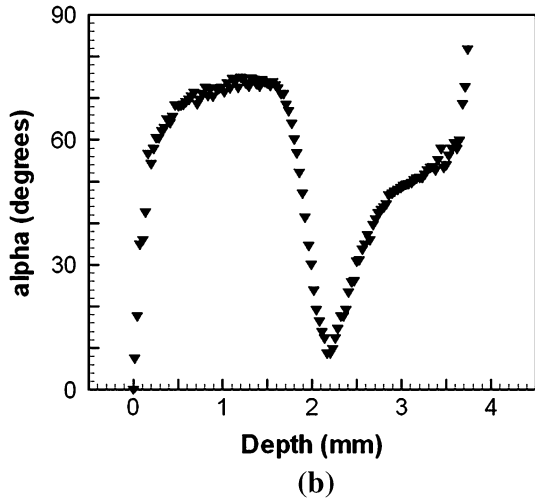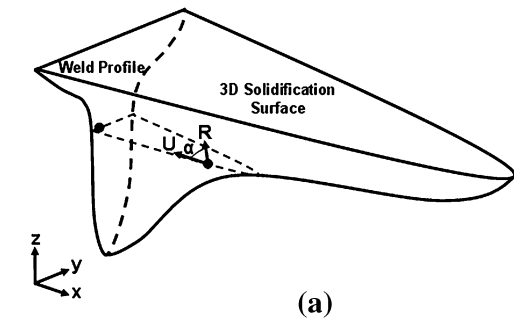
(a)

(b)

Fig. 1—The 3D solidification surface and resulting weld profile, (*a*), and variation of the angle α with depth along the central longitudinal plane for a 2.8 kW weld, (*b*), are shown. Also shown is the relationship between the welding speed, *U*, the solidification rate, *R*, and angle between the two vectors, α.

(a)

(b)

(c)

Fig. 2—The calculated molten pool profiles during keyhole mode laser welding are shown at different laser powers, (*a*) 1.0 kW, (*b*) 2.8 kW, and (*c*) 4.7 kW. The boiling point, liquidus temperature, and solidus temperatures are 3085 K, 1650 K, and 1616 K (2812 °C, 1377 °C, and 1343 °C), respectively. The fluid velocity reference vector of 500 mm s^{-1} is also shown.

are elongated reaching lengths of 60 μm or longer. While not observable in Figure 4, some cells grew perpendicular to the transverse plane. On the other hand, columnar dendrites are located near the center of the weld finger and are much coarser than the cells with dendrite arm sizes of 4 to 5 μm. The middle and right hand side portion of Figure 4(b) shows well developed columnar dendrites, and left hand side shows tertiary dendrites and the weld centerline.

A broader overview of the 2.8 kW weld fusion zone along with the calculated solidification direction (*i.e.*, $-\nabla T$) is given in Figure 5. Overall, the general wineglass shape of keyhole mode laser welds is observed as well as some porosity near the bottom of the weld due to keyhole instability. In terms of cell, dendrite, and grain orientation, the direction of growth is a function of position in the weld. The calculated orientation vectors are shown as unit vectors, so in 3D, the vectors have the same magnitude. Small vectors indicate significant growth in the *x*-direction, perpendicular to the page. In the middle part of the weld finger, mainly horizontal growth dominates. For rest of the weld, the solidification structures grow vertically towards the top surface of the workpiece but to different degrees. At the top of the weld, growth is at 45 deg to the horizontal, while at the weld root growth is almost vertical.
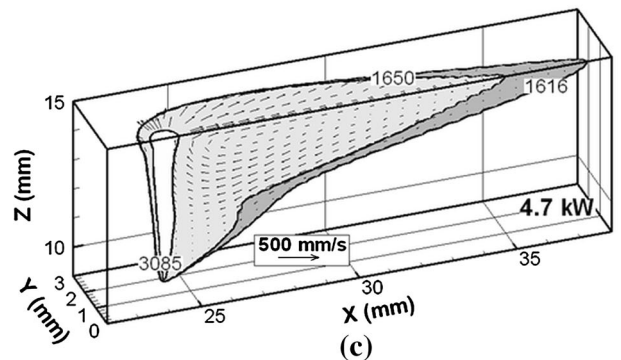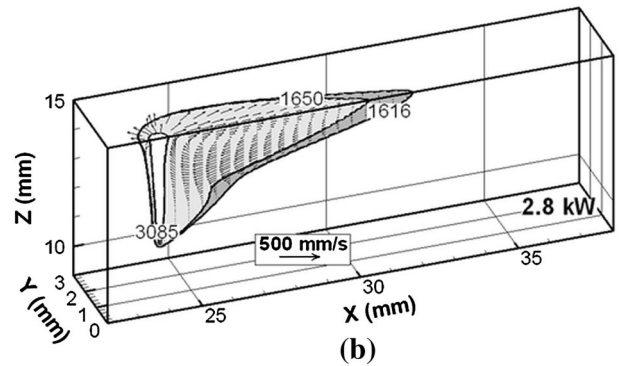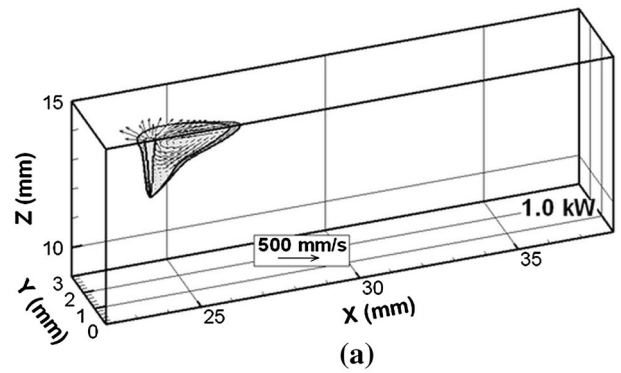
The large spatial variation of solidification structure size and morphology in both the whole fusion zone and individual micrographs is illustrated in Figures 5(b) through (d). Part b shows the microstructure near the top of the weld. Cells and dendrites exist together in this micrograph with cells towards the left and dendrites in the center and towards the right. This spatial variation indicates that the morphology parameter G/R is decreasing from left to right in Figure 5(b). The orientation of growth becomes steeper from the fusion line to the center of the weld. Figure 5(c) also shows both cells and dendrites, but variation in scale is clear. Individual cells are barely resolved at the fusion line, while relatively large dendrite arms can be seen at the centerline. This observation indicates that the cooling rate has decreased dramatically from the fusion line to the centerline.
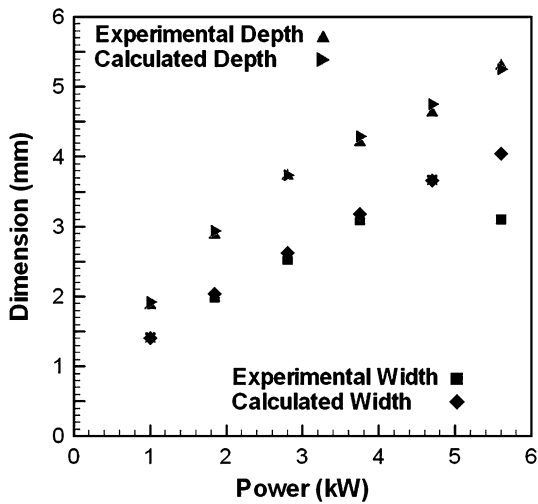
Fig. 3—The calculated and experimental molten pool dimensions are shown as a function of laser power for a travel speed of 34 m s^{-1}. The experimental and calculated molten pool widths and depths show good agreement.
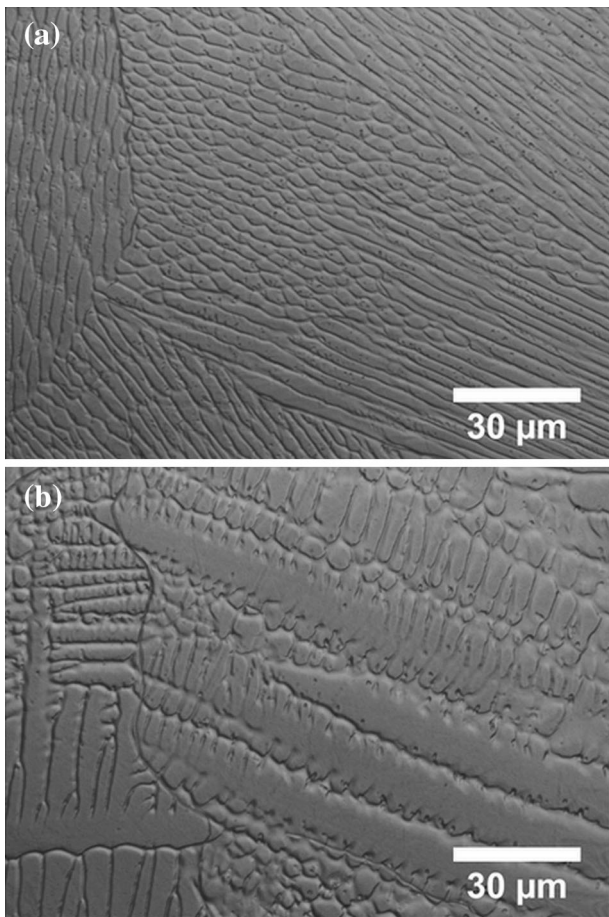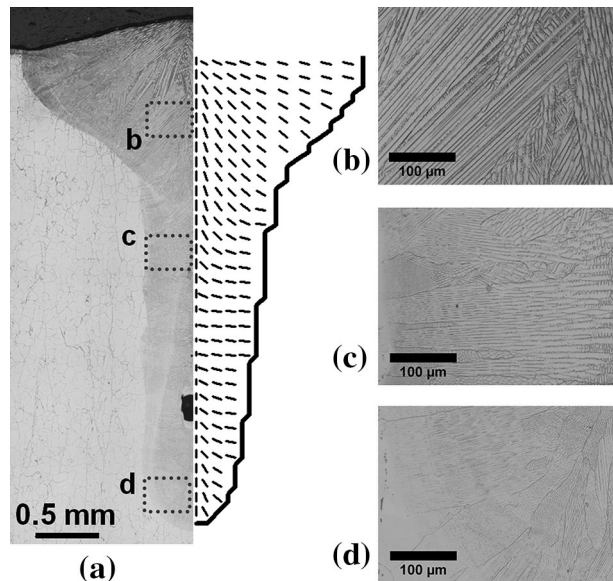

Fig. 5—The scale, mode, and orientation of solidification varies across the transverse section of the 2.8 kW weld. In (a) the general profile is shown with the positions of (b), (c), and (d) highlighted with rectangles. The calculated orientation of the solidifying cells, dendrites, and grains are shown in (a) based on the direction of heat flow at those positions.

Fig. 4—The solidification structures observed in this study are (a) cells and (b) dendrites. The cells and dendrites near the root and center of the fusion zone, respectively, of a 3.8 kW weld are shown.

Significant horizontal columnar dendrite growth is shown in Figure 5(c). Only fine cells growing in a nearly vertical direction are observed in Figure 5(d). This

observation indicates relatively high values of GR and G/R are expected.

Qualitatively, the observed growth directions and calculated growth directions agreed well, indicating that the experimental and calculated heat transfer directions are quite close. While observation of the fusion zone indicates that G/R varied enough to produce cells and columnar dendrites, the variation was not significant enough to produce equiaxed dendrites or significant amounts of planar solidification, which is observable just at the edge of the fusion zone in Figure 5. With typical values for alloying element diffusion in liquid metal, the minimum G/R value necessary for planar solidification can be estimated[15] and is on the order of 7000 K s mm^{-2}. So, based on experimental observations, G/R is at least 7000 K s mm^{-2} at the edge of the fusion zone, but at all other locations, the value is less.

B. Solidification Parameters

Figure 6 illustrates the variation of G and R as a function of depth along the central x–z plane in a 2.8 kW weld. The weld pool profile along the central longitudinal plane is shown as well in order to demonstrate how the shape of the solidification front affects the solidification parameters. The direction of heat transfer, which is aligned to the solidification direction, can be discerned by the slope of the liquidus contour [1650 K (1377 °C)]. A more vertical slope (i.e., the surface normal is closer aligned to the weld direction) produces a higher solidification rate. If the slope is close to zero, or the liquidus contour is nearly horizontal, the solidification rate is low. The magnitude of temperature gradient is qualitatively represented by how close the
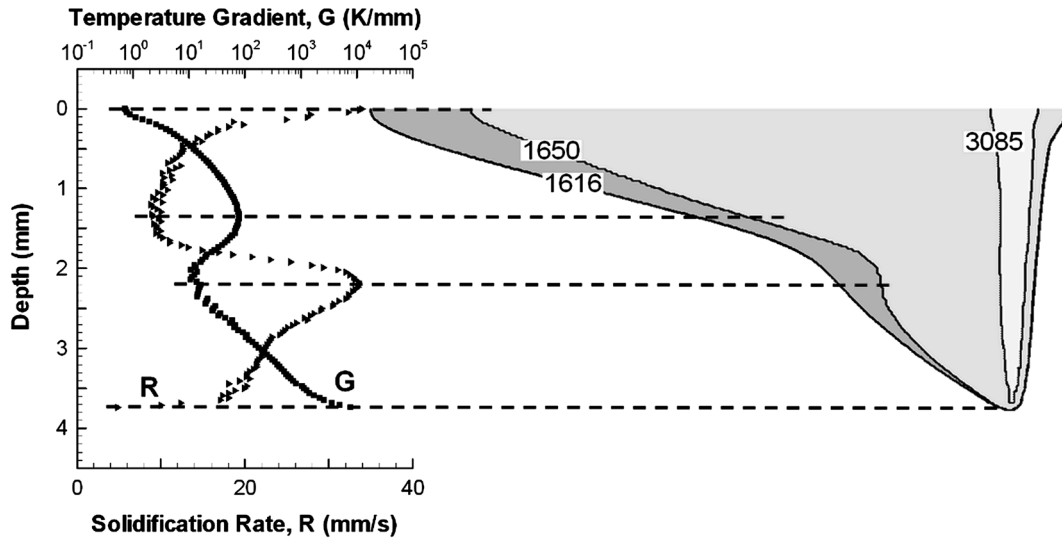
Fig. 6—The behavior of G and R as a function of depth along the central longitudinal plane for a 2.8 kW weld. The slope of the liquidus contour represents the solidification rate (i.e., larger absolute slope, greater R), and the distance between the solidus and liquidus contours corresponds to the temperature gradient (i.e., larger distance, lower G).

solidus and liquidus lines are to one another, or, alternatively, the width of the mushy zone. A larger mushy zone is associated with a lower temperature gradient.

In Figure 6, the slope of the liquidus contour and the width of the mushy zone decrease from the top to half the depth of the weld, which is represented by the increase in the temperature gradient and decrease in solidification rate. This behavior is typically observed in ellipsoidal weld pools produced by arcs and low intensity lasers.[36,37] However, due to the nature of the keyhole heat source, which extends into the depth of the weld pool, at half the depth along the weld centerline, both the verticality of the liquidus contour and mushy zone width increase sharply. This change results in a decrease of G and increase of R. These two characteristics, mushy zone width and liquidus contour slope, then decrease again as the liquidus contour approaches the bottom of the keyhole. Along the central x–z plane, the temperature gradient varies over four orders of magnitude from the top of the weld to the bottom, and the shapes of these two curves will impact the combined forms of G and R.
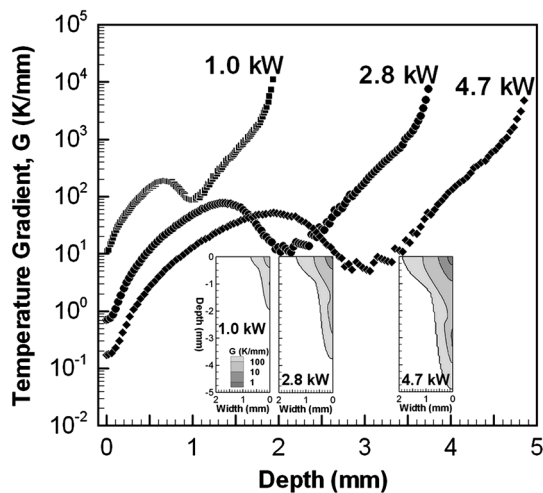
The temperature gradient (G) and solidification rate (R) along the central x–z plane for powers of 1.0, 2.8, and 4.7 kW and a travel speed of 34 mm s^{-1} are shown in Figure 7. Two-dimensional plots of G and R for the same powers are also shown. Each G curve exhibits a local minimum and maximum along the depth, and an increase in power tends to shift the curve down and increase the range over which G varies. For example, in the case of the 1 kW weld, the range over which G varies is three orders of magnitude, 10 to 10,000 K mm^{-1}, but for the 4.7 kW weld, G varies over four orders of magnitude from 0.2 K mm^{-1} at the top of the weld pool to 5000 K mm^{-1} near the bottom of the keyhole. A review of the temperature gradient plots inset in Figure 7(a) shows that increasing the power does not simply result in a larger weld profile with similar

contours. At higher powers, lower temperature gradients and a higher degree of spatial variation are observed throughout the weld. Additionally, the higher temperature gradients are found near the fusion line and root of the weld, while the lower values are found near the top center.

In Figure 7(b), the solidification rate, R, varies from 4 to 34 mm s^{-1} (the welding speed). Similar to the G plots, a local minimum and maximum are observed. Power does not appear to have a significant effect on R at the central longitudinal plane. However in the 2D R plots, relatively lower solidification rates are observed at higher powers. In the 4.7 kW weld, R is mostly 5 mm s^{-1} or more at the top half, where in the 1.0 kW weld R is 20 mm s^{-1} or more. Along the cross section, R decreases from the center of the weld to the fusion line because the surface normal vector is becoming increasingly misaligned with the travel direction.

Both G and R exhibit complex behavior as a function of position along the solidification front and a high degree of spatial variability, which will lead to variability in the parameters that control solidification structure scale and morphology. Figure 8 shows GR and G/R as a function of depth along the central x–z axis and cross sections for 1.0, 2.8, and 4.7 kW. The shapes of the curves are similar to the previous plots of G and R with a local minimum and maximum near the half depth of the weld, and the curves tend to shift to lower values when the power increases. However, the values of GR and G/R are varying over four to five orders of magnitude. For 4.7 kW, the cooling rate varies from 6 to 40,000 K s^{-1}, and G/R varies from 0.005 to 600 K s mm^{-2}. The large spatial variation in cooling rates and G/R values explains the variation in scale and morphology observed in Figure 5.

The effect of laser power on the cooling rate can be observed in the inset contour plots. At 1.0 kW most of the weld is cooling at rates above 1000 K s^{-1}, but as the
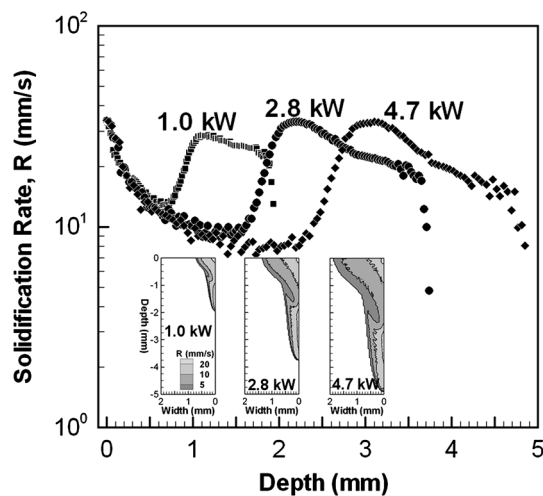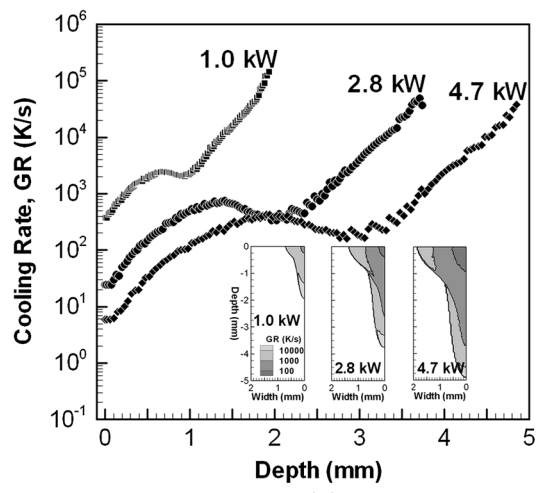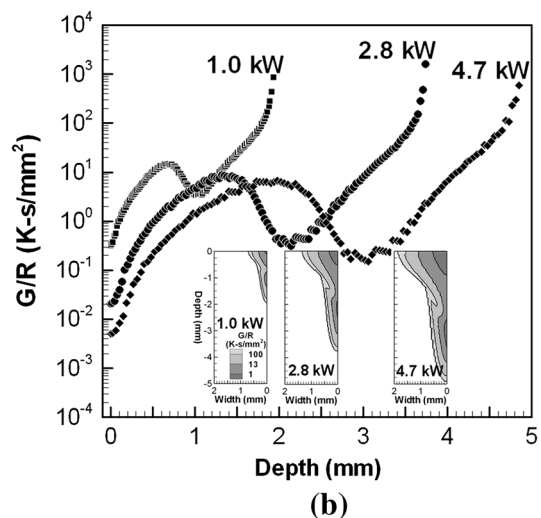
Fig. 7—The solidification parameters, (a) temperature gradient (G) and (b) solidification rate (R), are plotted as a function of depth along the central x–z plane and in 2D contour plots for various powers.

Fig. 8—The combined forms of solidification rate and temperature gradient, (a) cooling rate (GR) and (b) morphology parameter (G/R), are plotted as a function of depth along the central x–z plane and in 2D contour plots for various powers.

power increases, significant parts of the weld are cooling at rates less than 1000 K s^{-1}. At the highest power, a large section of the top of the weld is cooling at less than 100 K s^{-1}. The 2D G/R plots also show the effects of power on the distribution of the solidification structure morphology. The G/R contour of 13 K s mm^{-2} is chosen because it is close to the transition value from cellular to columnar dendritic morphologies, so at values less than 13 K s mm^{-2}, the morphology is likely to be dendritic. As power increases, the amount of the weld enclosed by the transition value contour increases, which means the area of the fusion zone containing dendritic structures should increase. Another observation of the same contour shows that it is not continuous along the depth for the 1 kW weld, indicating that transitions from dendrites to cells to dendrites may be observable at the center of the fusion zone.

The calculated solidification rates shown in Figure 8(a) are greater than 10 mm s^{-1} in most cases indicating that

rapid solidification may play an important role in the fusion zones of these welds.[38] A calculation considering a Ni-30 wt pct Cr binary system shows that the undercooling is within the experimental range consistent with equilibrium solidification. If the thermal and kinetic undercooling are neglected, the total undercooling, ΔT, can be determined by[39]

$$\Delta T = \Delta T_{\mathrm{C}} + \Delta T_{\mathrm{R}} = \frac{DG}{R} - \frac{m_{\mathrm{L}} R r (1-k) C_0}{D} + \frac{2\phi}{r}, \quad [5]$$

where ΔT_{C} is the constitutional undercooling, ΔT_{R} is the undercooling due to curvature, D is the diffusion coefficient for chromium in molten nickel,[40] G/R is the morphology parameter, m_{L} is the slope of the liquidus line in the Ni-Cr binary phase diagram, R is the solidification rate, r is the radius of curvature of the growing cell or dendrite, k is the distribution coefficient in the Ni-Cr system,[41] C_0 is the composition of the Ni-Cr alloy, and ϕ is the Gibbs–Thomson coefficient. The G/R value is taken from Figure 8(b) for values at high

Table III. The Values Necessary for the Undercooling Calculation are Given

D Ref. [40]	G/R	m_L Ref. [41]	R	r Ref. [38]	k Ref. [41]	C_0	φ Ref. [38]
5×10^{-9} (m^2 s^{-1})	10^6 (K s m^{-2})	-2 (K/wt pct Cr)	0.034 (m s^{-1})	5×10^{-8} (m)	0.55	30 (wt pct Cr)	10^{-7} (K m)

solidification rates. The value for the radius of curvature and Gibbs–Thomson coefficient are typical values from Kurz and Fisher.[38] For the values given in Table III, the undercooling is 13 K. Kraus[42] measured undercoolings as high as 30 K in stainless steel weld pools, where equilibrium solidification was observed. Due to the low calculated undercooling, the effects of rapid solidification were not included in the model.

C. Scale of the Solidification Structures

The size and scale of cells and dendrites are known to vary as a function of cooling rate.[15] The cooling rate varied significantly over the range of laser powers investigated. The measured cell and secondary dendrite arm spacings were correlated to the calculated cooling rates (GR) at various positions in the weld cross section. Figure 9 shows the effect of the calculated cooling rate on experimental cell spacing and secondary dendrite arm spacing. The n value, which is defined as

$$\log(\text{spacing}) = n \log(GR) + \log(b) \quad [6]$$

is provided for each structure. The relation in Eq. [6] is well established in the study of secondary arm spacings and is based on the solidification time being inversely proportional to the cooling rate.[15] A more detailed description by Kurz and Fisher,[38] which uses a similar relation, assumes competing growth between two cylinders (i.e., secondary dendrite arms).

In Figure 9, the cell spacing ranges from 3.9 μm at 8000 K s^{-1} to 1.7 μm at 90,000 K s^{-1}. The secondary dendrite arm spacing varies from 4.0 μm at 200 K s^{-1} to 1.4 μm at 7000 K s^{-1}. These data compare well to similar data for 201 stainless steel.[43] Additionally, the measured cell and secondary arm spacings from the literature for Alloy 690 showed cell and dendrite arm spacings of about 4 μm for comparable heat inputs.[8,10] The data points shown in Figure 9 represent a combination of 87 and 58 linear intercept measurements for cells and dendrite arms, respectively. The standard deviations for the measurements vary from 0.06 to 1.01 μm. Median standard deviations are 0.35 and 0.28 μm for cell and secondary dendrite arm spacings, respectively, and are comparable to the standard deviations of similarly sized stainless steel spacing measurements.[35]

The following relations give the size of the solidification structures in microns as a function of cooling rate (K s^{-1}) in the general form $\lambda = b(GR)^n$, based on the fitted lines in Figure 9

$$\lambda_{CS} = 60.6(GR)^{-0.31}, \quad [7]$$
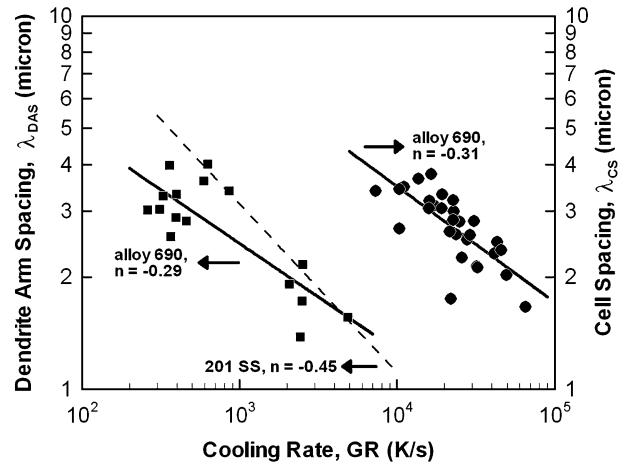
$$\lambda_{DAS} = 17.9(GR)^{-0.29}, \quad [8]$$

Fig. 9—The measured cell spacing (circles) and secondary dendrite arm spacing (squares) are shown as a function of calculated cooling rate. The 201 stainless steel[43] system is shown for comparison.

where λ_{CS} is the cell spacing and λ_{DAS} is the secondary dendrite arm spacing. These cooling rate relations are much more precise than any heat input relations since, as demonstrated previously, the cooling rate can vary significantly as a function of position in a weld pool for any given heat input. These data are not limited to just laser welding and can be applied to various processes that require or incorporate solidification processing, including casting, conventional arc welding, and other high energy beam processes.

D. Morphology of the Solidification Structures

The parameter G/R, which determines the morphology of the solidification structure, can be calculated and correlated to the experimental microstructure in the fusion zone. In the fusion zone, the solidification structure consisted mostly of cells and columnar dendrites since significant amounts of equiaxed dendrites and planar solidification were not observed. The area fractions of cells and columnar dendrites were measured by optical microscopy. The values of G/R were correlated with the observed solidification structure in the fusion zone. The computed G/R values were 13 K s mm^{-2} or lower in all areas where columnar dendrites were observed. Similarly, the computed G/R values were 21 K s mm^{-2} or higher where cellular structure was observed. The transition between columnar dendrites and cellular structure occurred between 13 and 21 K s mm^{-2}. By using the value of G/R that corresponds to the cells and columnar dendrites, the area fractions of the two solidification structures in the transverse cross-section of the weld can be calculated.
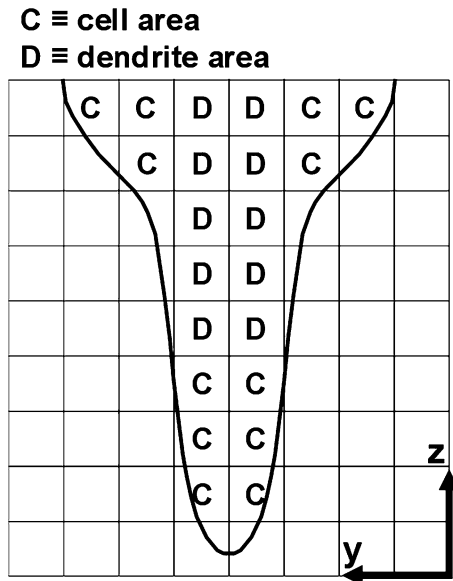
C ≡ cell area
D ≡ dendrite area

Fig. 10—A schematic of the calculated fusion zone shows how the area fractions of cells and dendrites are calculated. If the calculated G/R value of a given control volume is greater than the critical value, then the area of the y–z face is assigned to the cell area fraction. Otherwise, the area is added to the dendrite area fraction.
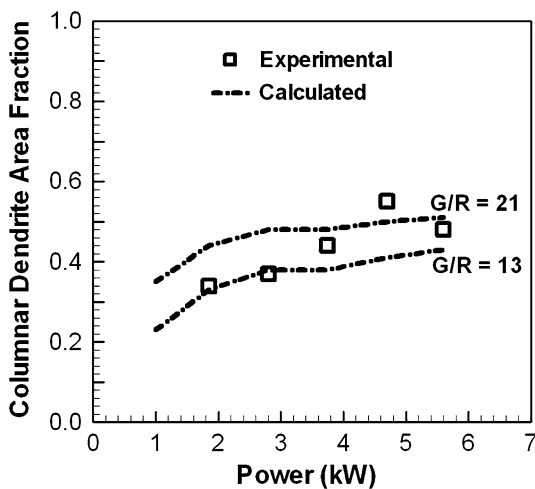

Fig. 11—A comparison between the calculated and experimental area fractions of columnar dendrites shows good agreement. The different G/R values represent the lowest value at which cells were observed and greatest value where columnar dendrites were observed.

A transverse cross section of the fusion zone is shown in Figure 10. If the G/R value is less than the critical value for the transition from dendrites to cells, then the y–z face of the control volume is assigned to the dendrite area, or D in the schematic. In this way the total area of cells and dendrites is determined. The area fractions are the areas of cells or dendrites divided by the total area. Figure 11 shows the experimental and calculated fusion zone area fractions of columnar dendrites with two different critical G/R values. Only the fraction of cells and columnar dendrites are considered, since significant amounts of equiaxed dendrites and planar solidification were not observed. For the conditions examined in this
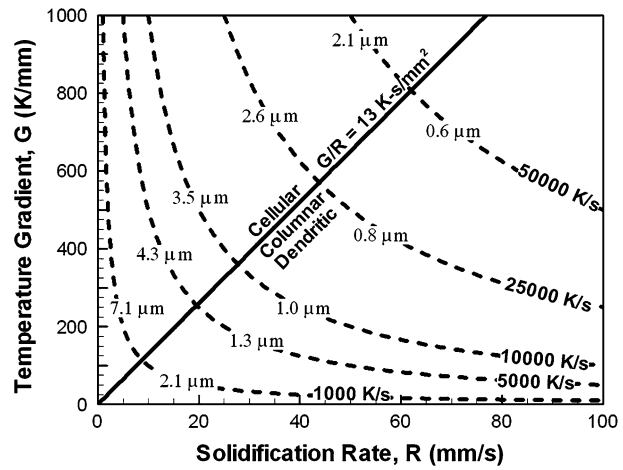

Fig. 12—The solidification map shows the transition from cellular to columnar dendritic morphology with various cooling rates. Along each cooling rate is the cell spacing and secondary dendrite arm spacing, which are determined from Eqs. [5] and [6]. With this map the scale and morphology of the solidification structures can be predicted quantitatively.

study, the area fraction of columnar dendrites barely exceeds 0.5 for a laser power of 4.7 kW. The model calculations and experimental measurements agree.

The size and morphology of the solidification structures within the experimental welds have been correlated to calculate solidification parameters. A solidification map for Alloy 690 can now be constructed to predict the solidification morphology and the scale of the structure. This map is shown in Figure 12. The solid straight line delineates the cellular and columnar dendritic regions of the map. Cooling rates are represented by the dashed curved lines and show the cell spacings and secondary dendrite arm spacings calculated from Eqs. [5] and [6], respectively. This map has a number of practical applications. For any given welding parameters, the minimum size of secondary arm spacings can be determined immediately based on the welding speed since the solidification rate can not exceed the welding speed. For example, if the welding speed is set to 25 mm s^{-1}, then a secondary arm spacing of 1.3 μm is possible, while a value of 1.0 μm is not. On the other hand, cell spacings greater than 2.6 μm would be expected for most of the weld, where the temperature gradient is 1000 K mm^{-1} or less. Spacings less than 2.6 μm would be confined to high temperature gradient and cooling rate regions, such as the root of the weld and near the fusion line. In addition, the wide range of G and R values makes the map applicable to any process, where solidification processing of Alloy 690 is necessary.

IV. SUMMARY AND CONCLUSIONS

The solidification parameters of Inconel® Alloy 690 during keyhole mode laser welding have been calculated using a mathematical model, and correlated with experimentally determined solidification structure. The large variation in the solidification parameter values in the fusion zone of the laser welds allowed for the construction

of a solidification map that describes the scale and morphology of the solidification structures for given values of G and R.

1. A large spatial variation of the calculated solidification parameters was observed. Along the central longitudinal plane, the G/R value could vary up to five orders of magnitude. In both the transverse cross section and the central longitudinal plane, increases in laser power lead to a significant increase in the spatial variation of the solidification parameters.
2. The measured cell and secondary dendrite arm spacings were correlated to the calculated solidification parameters and expressed as functions of cooling rate in the form $\lambda = b(GR)^n$. These expressions can be applied for a variety of welding processes and conditions. G/R values of 13 and 21 K s mm^{-2}, which are associated with the transition from cellular to columnar dendritic solidification structures, were used to calculate the dendrite area fractions, which agreed with the measured values.
3. A map of solidification scales and morphologies for Alloy 690 was constructed based on the data presented in this work. The cell and dendrite arm sizes and the cellular and dendritic morphology regions are plotted as a function of the temperature gradient, G, and the solidification rate, R. The utility of the map was highlighted by describing how minimum secondary dendrite arm spacings can be selected based on the welding speed. Due to the large range of G and R values captured in these keyhole mode laser welds, the map has very wide applicability to a range of materials processes from casting to arc and laser welding.

REFERENCES

1. Q.Z. Zuo, F. Liu, L. Wang, and C. Chen: *Metall. Mater. Trans. A*, 2013, vol. 44A, pp. 3014–27.
2. F. Azarmi and C.P. Leither: *Metall. Mater. Trans. A*, 2012, vol. 43A, pp. 4703–10.
3. M. Xie, R. Helmink, and S. Tin: *Metall. Mater. Trans. A*, 2012, vol. 43A, pp. 1259–67.
4. C.L. Brundidge, D. Vandrasek, B. Wang, and T.M. Pollock: *Metall. Mater. Trans. A*, 2012, vol. 43A, pp. 965–76.
5. T.D. Anderson, J.N. DuPont, and T. DebRoy: *Acta Mater.*, 2010, vol. 58, pp. 1441–54.
6. T. Allen, J. Busby, M. Meyer, and D. Petti: *Mater. Today*, 2010, vol. 13, pp. 14–23.
7. S. Fukumoto and W. Kurz: *ISIJ Int.*, 1999, vol. 39, pp. 1270–79.
8. G.J. Abraham, R. Bhambroo, V. Kain, G.K. Dey, and V.S. Raja: *J. Mater. Eng. Perform.*, 2013, vol. 22, pp. 427–32.
9. S.-L. Jeng and Y.-H. Chang: *Mater. Sci. Eng. A*, 2012, vol. 555, pp. 1–12.
10. H.T. Lee and J.L. Wu: *Corros. Sci.*, 2009, vol. 51, pp. 439–45.
11. H.T. Lee and T.Y. Kou: *Sci. Technol. Weld. Join.*, 1999, vol. 4, pp. 246–56.
12. T.-Y. Kou, H.T. Lee, and C.C. Tu: *Sci. Technol. Weld. Join.*, 2003, vol. 8, pp. 39–48.
13. T.-Y. Kou and H.-T. Lee: *Mater. Sci. Eng. A*, 2002, vol. 338, pp. 202–12.
14. A. Raghavan, H. Wei, T.A. Palmer, and T. DebRoy: *J. Laser Appl.*, 2013, vol. 25, art. no. 052006.
15. S. Kou: *Welding Metallurgy*, 2nd ed., Wiley, Hoboken, NJ, 2003.
16. W. Zhang, G.G. Roy, J.W. Elmer, and T. DebRoy: *J. Appl. Phys.*, 2003, vol. 93, pp. 3022–33.
17. R. Rai, G.G. Roy, and T. DebRoy: *J. Appl. Phys.*, 2007, vol. 101, art. no. 054909.
18. R. Rai, J.W. Elmer, T.A. Palmer, and T. DebRoy: *J. Phys. D*, 2007, vol. 40, pp. 5753–66.
19. R. Rai, S.M. Kelly, R.P. Martukanitz, and T. DebRoy: *Metall. Mater. Trans. A*, 2008, vol. 39A, pp. 98–112.
20. T.D. Anderson, J.N. DuPont, and T. DebRoy: *Metall. Mater. Trans. A*, 2010, vol. 41A, pp. 181–93.
21. J.D. Hunt: *Mater. Sci. Eng.*, 1984, vol. 65, pp. 75–83.
22. M. Gaumann, R. Trivedi, and W. Kurz: *Mater. Sci. Eng. A*, 1997, vols. 226–228, pp. 763–69.
23. M. Gaumann, C. Bezencon, P. Canalis, and W. Kurz: *Acta Mater.*, 2001, vol. 49, pp. 1051–62.
24. W. Tan, N.S. Bailey, and Y.C. Shin: *J. Manuf. Sci. Eng.*, 2012, vol. 134, p. 041010.
25. W. Zhang, C.-H. Kim, and T. DebRoy: *J. Appl. Phys.*, 2004, vol. 95, pp. 5210–19.
26. H. Zhao and T. DebRoy: *J. Appl. Phys.*, 2003, vol. 93, pp. 10089–96.
27. B. Ribic, R. Rai, and T. DebRoy: *Sci. Technol. Weld. Join.*, 2008, vol. 13, pp. 683–90.
28. B. Ribic, S. Tsukamoto, R. Rai, and T. DebRoy: *J. Phys. D*, 2011, vol. 44, art. no. 485203.
29. A. Kaplan: *J. Phys. D*, 1994, vol. 27, pp. 1805–14.
30. S. Krishnan and P.C. Nordine: *J. Appl. Phys.*, 1996, vol. 80, pp. 1735–42.
31. W.F. Gale and T.C. Totemeier: *Smithells Metals Reference Book*, 8th ed., Elsevier Butterworth-Heinemann, Burlington, VT, 2004.
32. Special Metals Corporation: *INCONEL® Alloy 690 Data Sheet, Publication Number SMC-079*, 2009, http://www.specialmetals.com/documents/Inconel%20alloy%20690.pdf, Accessed 9 July 2013.
33. L.B. Pakratz: *Thermodynamic Properties of Elements and Oxides*, U.S. Dept. of the Interior, Bureau of Mines, District of Columbia, 1982.
34. Y.V. Glagoleva, N.B. Pushkareva, Y.E. Lapshova, O.V. Sadyreva, V.R. Polev, V.I. Gorbatov, S.G. Taluts, and I.G. Korshunov: *Phys. Met. Metallogr.*, 2006, vol. 102, pp. 48–54.
35. M.A. Valiente-Bermejo, L. Karlsson, and T. DebRoy: *14th Nordic Laser Materials Processing Conference*, 2013, pp. 3–14.
36. W. Liu and J.N. Dupont: *Acta Mater.*, 2004, vol. 52, pp. 4833–47.
37. J.M. Vitek: *Acta Mater.*, 2005, vol. 53, pp. 53–67.
38. W. Kurz and D.J. Fisher: *Fundamentals of Solidification*, 3rd ed., Trans Tech Publications, Brookfield, VT, 1989.
39. S.A. David and J.M. Vitek: *Int. Mater. Rev.*, 1989, vol. 34, pp. 213–45.
40. S. Nikolic, A. Golubovic, V. Radojevic, A. Valcic, and B. Jordovic: *J. Metallr.*, 2004, vol. 10, pp. 289–93.
41. P. Nash: *Alloy Phase Diagrams*, ASM International, Materials Park, OH, 1991, vol. 3.
42. H.G. Kraus: *Weld. J.*, 1987, vol. 66, pp. S353–59.
43. A. Paul and T. DebRoy: *Metall. Trans. B*, 1988, vol. 19B, pp. 851–58.